Applied Geochemistry 147 (2022) 105515

Contents lists available at ScienceDirect

Applied Geochemistry

journal homepage: www.elsevier.com/locate/apgeochem

Atomic-scale characterisation of sodium aluminosilicate hydrates (N-A-S-H) and Mg-substituted N(-M)-A-S-H using XANES

Xinyuan Ke [a,*], Vahiddin Alperen Baki [a], Alexander I. Large [b], Georg Held [b], Brant Walkley [c], Jiaqi Li [d]

[a] Department of Architecture and Civil Engineering, University of Bath, Bath, BA2 7AY, UK
[b] Diamond Light Source Ltd., Harwell Science & Innovation Campus, Didcot, Oxfordshire, OX11 0DE, UK
[c] Department of Chemical and Biological Engineering, The University of Sheffield, Sheffield, S1 3JD, UK
[d] Atmospheric, Earth & Energy Division, Lawrence Livermore National Laboratory, Livermore, CA, 94550, USA

ARTICLE INFO

Editorial handling by Dr Dmitrii A. Kulik

Keywords:
Amorphous material
X-ray absorption spectroscopy
Atomic-level characterization
Alkali-activated geopolymer materials

ABSTRACT

The chemical structures of aluminosilicate hydrates presented in alkali-activated geopolymer materials underpin their performances. Mg-substituted sodium aluminosilicate hydrates (N(-M)-A-S-H) are likely to be present in alkali-activated geopolymer materials prepared using MgO-containing precursors, however, their atomic-level structures remain unclear. The lack of such knowledge made it challenging to identify and distinguish N(-M)-A-S-H from complex alkali-activated geopolymer systems (i.e., alkali-activated slag, alkali-activated Mg-rich minerals), and therefore brought challenges in understanding and predicting their durability. This study characterised for the first time the atomic structures of the synthetic N(-M)-A-S-H gels, prepared through ion-exchange or co-synthesis, using X-ray absorption near-edge spectroscopy (XANES) at Si, Al and Mg K-edge. The results suggest that the substitution of Mg in the extra-framework locations of the alkali aluminosilicate hydrates (N-A-S-H) leads to negligible changes in the coordination environments of the aluminosilicate framework. However, the Mg coordination environment is distinguishably different from other Mg-containing phases in the systems, e.g., hydrotalcite. The Mg K-edge XANES of N(-M)-A-S-H shows a 0.8–1.2 eV shift compared with hydrotalcite. The results presented in this study can be used as the fingerprint to probe the presence of N(-M)-A-S-H in alkali-activated geopolymer materials containing Mg element.

1. Introduction

Alkali-activated geopolymer materials play indispensable roles in a wide range of engineering applications as low-carbon sustainable materials that can provide matching performances (Provis et al., 2015; Zhang et al., 2021). They are predominately used as alternative building materials, but with emerging research and applications in fields such as nuclear waste encapsulation (Ke et al., 2019), wastewater treatment (Luukkonen et al., 2019), and energy storage (Ke and Baki, 2021). The alkali-activated materials are prepared by mixing alkali activators (i.e., NaOH, Na_2SiO_3, Na_2CO_3) with aluminosilicate precursors, where versatile aluminosilicate-rich inorganic materials, such as industrial by-products and mineral wastes, can be utilised (Bernal et al., 2013; Khalifa et al., 2020; Provis et al., 2015). When aluminosilicate precursors with low Ca and Mg content (<10 wt%) and sodium-based alkali solutions are used, the amorphous sodium aluminosilicate hydrates (N-A-S-H) form as the main reaction products (García-Lodeiro et al., 2010; Ke and Duan, 2021).

These amorphous sodium aluminosilicate hydrates consist of tetrahedrally-coordinated framework aluminosilicate gels with pseudo-zeolitic nanoscale structures (Provis et al., 2005; Walkley et al., 2021), where the sodium cations serve as the extra-framework cation charge balancing the tetrahedrally coordinated aluminium ($Al^{[4]}$) in the aluminosilicate framework. Similar to the crystalline aluminosilicate zeolites, these extra-framework cation sites can also be taken by other cations, either via co-precipitation during the initial geopolymerisation stage or through ion-exchange after the solidification of the main aluminosilicate framework (Ge et al., 2015; Walkley et al., 2019). These cations also play important roles in determining and modifying the atomic-level aluminosilicate framework structures (Walkley et al., 2019), as well as affecting their mesoporous pore structures and water sorption behaviours (Ke and Baki, 2021).

* Corresponding author.
E-mail address: x.ke@bath.ac.uk (X. Ke).

https://doi.org/10.1016/j.apgeochem.2022.105515
Received 5 June 2022; Received in revised form 17 October 2022; Accepted 9 November 2022
Available online 12 November 2022

In comparison with monovalent cations (i.e., Na^+ and K^+), the addition of even a small amount of multivalent cations can lead to modification/distortion of the aluminosilicate framework, likely due to the different ionic radii and electrostatic forces between Na^+ and multivalent cations (García-Lodeiro et al., 2010; Walkley et al., 2019). Divalent cations, particularly Ca^{2+} and Mg^{2+}, are commonly present in the aluminosilicate precursors used for the synthesis of alkali-activated geopolymer materials, therefore, it is crucial to understand the fate of these elements in the alkali-activated geopolymer materials. The Ca-substituted sodium aluminosilicate hydrates N(-C)-A-S-H have been prepared and systematically assessed in literature using the co-precipitation method, where the Ca substitution content were limited to below 10 wt% (García-Lodeiro et al., 2010; Garcia-Lodeiro et al., 2011). As for Mg, magnesium silicate hydrates (M-S-H) were observed to form in alkali-activated nickel slag with MgO content higher than 25 wt % (Yang et al., 2019), while a new amorphous magnesium silicate phase (unnamed) was observed to form in alkali-activated aluminosilicate glasses with Mg content up to 30 wt% (Sreenivasan et al., 2021). However, although partially crystallized aluminosilicate phases (poorly crystallized zeolites) were also identified in these studies, the possibility of having Mg present as extra-framework cation of aluminosilicate hydrates (N(-M)-A-S-H) has not been considered. As the atomic level structure of N(-M)-A-S-H gels have not yet been revealed, probing this phase in complex alkali-activated materials, such as alkali-activated slags, would be extremely challenging if not impossible.

The atomic-level changes of the alkali aluminosilicate hydrates (N-A-S-H) impact the performances of alkali-activated geopolymer materials for different engineering applications, through controlling of their bulk physical chemical properties and long-term crystalline structures (Ke et al., 2019; Longhi et al., 2022). In particular, the presence of Mg-substituted N(-M)-A-S-H gels might impact the long-term durability, surface properties and leachabilities of the geopolymer materials, which are relevant to their applications in construction, as well as nuclear waste encapsulation and management (Vespa et al., 2020). The lack of understanding of the coordination environment of Mg in the Mg-substituted N(-M)-A-S-H gels will also add challenges to the characterisation and interpretation of the bulk alkali-activated materials prepared from Mg-containing precursors, such as alkali-activated slag and alkali-activated Mg-rich minerals.

X-ray absorption near-edge spectroscopy (XANES) is an analytical tool used to probe the local electronic structure of an atom of interest (Calas et al., 1987). It is particularly powerful to elucidate the coordination environment of 1) poorly crystalline phases or complexes (e.g., cementitious gels) which cannot be determined using X-ray diffraction 2) elements of interest (e.g., Mg, Si, and Ca) with low natural abundance for nuclear magnetic resonance spectroscopy (Calas et al., 1987; Ildefonse et al., 1995; Li et al., 2021b; Vespa et al., 2018). Recent advances in XANES allow its application in cement-related studies. The coordination environment of Ca, Al, and/or Si of phases in Portland cement, calcium aluminate cement, oil-well cement, and supplementary cementitious materials have been extensively studied (Geng et al., 2018; Li et al., 2020, 2021b; Vespa et al., 2018, 2020). These studies pave the way for the investigation of other complex cementitious systems, including the alkali-activated geopolymer materials. Nevertheless, the coordination environment of Si, Al and Mg in the main geopolymer component N-A-S-H and the Mg-substituted N(-M)-A-S-H have rarely been explored in this research community. A systematic study of these phases as a brief database would lay a foundation for further XANES application in cement and concrete research.

In this study, the atomic-level chemical coordination of Mg-substituted sodium aluminosilicate hydrates N(-M)-A-S-H were probed using the X-ray absorption near-edge spectroscopy (XANES) at Mg, Si and Al K-edge. N-(M)-A-S-H gels synthesised using both external ion-exchange and internal co-synthesis processes were assessed, and the effect of different Si/Al ratios on the structure of amorphous aluminosilicate gels have also been discussed.

2. Materials and methods

2.1. Sample preparations and characterisation

In this study, alkali-activated metakaolin geopolymer is used to synthesize the amorphous sodium aluminosilicate hydrate gels (N-A-S-H), prepared by mixing aqueous alkali solutions with metakaolin (MetaStar 501, Imerys UK) to obtain a stoichiometry of $Na_2O{\cdot}Al_2O_3{\bullet}nSiO_2{\bullet}13H_2O$. Two siliceous activators (room temperature), prepared from NaOH (Honeywell Fluka, ≥98%) pellets and sodium silicate solution (PQ Corporation, 26.5 wt% SiO_2 and 10.6 wt% Na_2O), were used to synthesize N-A-S-H gels with bulk Si/Al ratio of 1.7 and 1.5. The required amount of deionised water was added to the alkali-activator solution to obtain a constant water to cation molar ratio in each sample. The mixtures were blended using a high shear overhead mixer, cast and sealed in centrifuge tubes, and stored at 20 °C for 28 days prior to analysis.

The Mg-substituted sodium aluminosilicate hydrates N-(M)-A-S-H were prepared using two different routes, ion-exchange and co-synthesis. For the ion-exchange route, the N-A-S-H gels prepared from metakaolin geopolymer (at the age of 28 days) were mixed with 0.5 mol/L $Mg(NO_3)_2$ solution with a liquid to solid ratio of 100:1. The $Mg(NO_3)_2$ solution was prepared by dissolving $Mg(NO_3)_2{\bullet}6H_2O$ (Scientific Laboratory Supplies) in deionised water. The solid-liquid mixtures were regularly shaken every day for 14 days before being separated. The separated wet solids were washed by deionised water to remove surface $Mg(NO_3)_2$, and then dried in the 105 °C oven overnight. A previous study by White et al. (2010) shows that the drying temperature applied in this study would only lead to negligible structural changes and is therefore appropriate for this study. The ion-exchanged N(-M)-A-S-H gels are denoted by "N(-M)-A-S-H1.5" and "N(-M)-A-S-H 1.7" for designed bulk Si/Al ratio of 1.5 and 1.7.

For the co-synthesis method, 10% of the Na_2O content in the original stoichiometry geopolymer design was replaced by the MgO. Therefore, an activator with part of the Na_2O content replaced by the MgO content was prepared, keeping the total positive charge from the cation and the total SiO_2 content constant. $Mg(NO_3)_2{\bullet}6H_2O$ salt was used to introduced Mg into the alkali-activator. When adding magnesium salt to the alkali activator, $Mg(OH)_2$ solids are likely to precipitate due to its low solubility. To avoid leaving significant amount of unreacted $Mg(OH)_2$ in the prepared N(-M)-A-S-H gels, only a low Mg replacement ratio was designed for the co-synthesis process. Prior to mixing with metakaolin, the solid NaOH pellets were dissolved in the as received sodium silicate solution and cooled down to room temperature. The $Mg(NO_3)_2{\bullet}6H_2O$ salt was dissolved in the deionised water (the additional amount of water required to satisfy the $H_2O/Al_2O_3 = 13$ mix design) and equilibrated at room temperature. The $Mg(NO_3)_2$ solution was then poured into the alkali solution to form a cloudy solution (instantly forming $Mg(OH)_2$ with negligible agglomeration) and quickly added to the metakaolin for co-synthesis of Mg-substituted sodium aluminosilicate hydrates N(-M)-A-S-H. The fresh state workability of the paste with added Mg sources was very similar to that of the sodium silicate activated geopolymer paste. The co-synthesised N(-M)-A-S-H gel was only prepared with bulk Si/Al ratio of 1.5 and denoted by "N(-M)-A-S-H1.5-CoSyn" in this study and characterised at the age of 28 days.

2.2. Testing methods

2.2.1. X-ray diffraction and elemental analysis

The crystallographic structure of the synthesised alkali aluminosilicate geopolymer gels were characterised using the powder X-ray diffraction (XRD), performed on a STOE STADI P (Cu radiation, $\lambda = 1.54$ Å) instrument in the transmission mode, operating at 40 kV and 40 mA. The diffraction patterns were recorded from 5° to 75° (2θ), with a step resolution of 0.015° (2θ) per step. A double Mythen detector was used, where each detector covers a range of 19° (2θ) and operated at 31.6 s per

degree (2θ), resulted in around 20 min for each XRD scan.

The chemical compositions of the synthesised alkali aluminosilicate geopolymer gels were characterised using the energy dispersive X-Ray analysis (SEM-EDX, Hitachi SU3900). The grounded alkali aluminosilicate geopolymer gel powders were dispersed onto the conductive carbon tape and stored under vacuum for 24 h to remove free water prior to the analysis. For each sample, 15 random locations were chosen for conducting the quantified EDX analysis, and the average chemical compositions based on these 15 locations were reported as the representative bulk chemical compositions.

2.2.2. X-ray absorption spectroscopy

The X-ray absorption near-edge spectra (XANES) around Mg, Si and Al K-edge were collected from the VerSoX beamline (B07) at the Diamond Light Sources (UK) (Held et al., 2020). The powdered samples were pressed onto conductive carbon tapes and mounted onto the sample holder. All experiments were carried out at room temperature under 0.5 mbar Ar gas atmosphere (to compensate charging of the samples) in total electron yield (TEY) detection mode. The electrons emitted from the sample were collected by an electrode at a distance of <1 mm from the sample. I_0 was recoded through a gold mesh inserted after the last mirror of the beamline. Data were recorded in steps of 0.2 eV. All XANES data were divided by I_0 and normalised with respect to the high-energy signal after the pre-edge background had been subtracted. The summary of all XANES data after normalisation can be found in the Supporting Information document. Quartz, carbonated hydrotalcite (>99.9%, Sigma Aldrich), and talc (>99%, Sigma Aldrich) were used as reference compounds for Si, Al and Mg K-edge spectra, where the edge energy (determined by the inflection point) values were characterised as 1824.4 eV (Si K-edge whiteline peak), 1548.8 eV (Al K-edge whiteline peak) and 1295.5 eV (Mg K-edge whiteline peak), respectively. In addition, the synthetic $CaSiO_3$ (>99% pseudowollastonite) and silica gel were purchased from Fisher Scientific. The synthetic ettringite and Ye'elimite are the same materials as reported in (Myers et al., 2017) and (Li et al., 2021a), respectively.

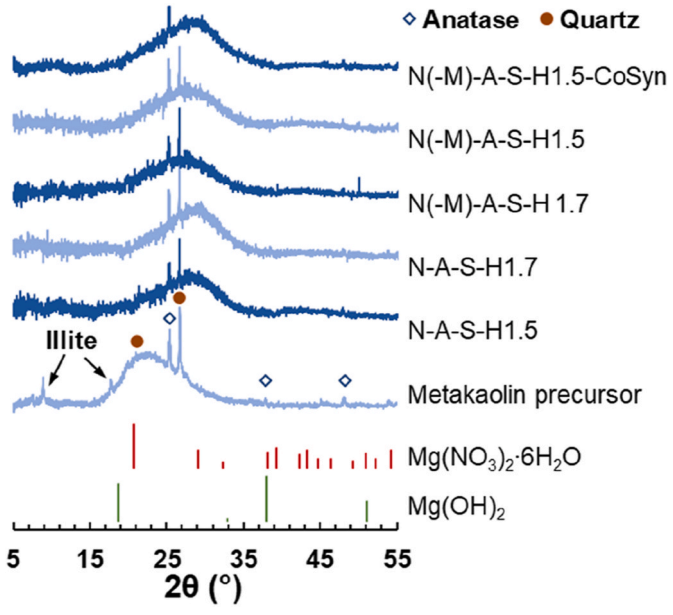

Fig. 1. X-ray diffraction patterns of the metakaolin precursor and the synthetic N-A-S-H and N(-M)-A-S-H gels. The standard diffraction patterns of Mg $(NO_3)_2$•$6H_2O$ (PDF# 44–0521) and $Mg(OH)_2$ (PDF# 84–2164).

3. Results and discussions

3.1. Crystallographic and elemental characterisation

Fig. 1 presents the crystallographic structure of the N-A-S-H and N(-M)-A-S-H gels prepared in this study, together with the mineralogy of the metakaolin precursor used as starting materials. The metakaolin precursor used in this study contains a small fraction of quartz (SiO_2, powder diffraction pattern, PDF# 01-078-2315), anatase (TiO_2, PDF# 01-084-1286), and illite (PDF# 00-026-0911) impurities. Apart from illite, the quartz and anatase impurities remained as unreacted impurities in the synthesised N-A-S-H and N(-M)-A-S-H gels, consistent with previous studies using metakaolin as precursors for producing geopolymers (Ke and Baki, 2021; Walkley et al., 2021). The reduction in intensity of the reflection peaks corresponding to quartz in the N(-M)-A-S-H1.5-CoSyn sample is likely due to preferred orientation during XRD characterisation causing changes in the relative intensities of the reflection peaks. As shown in Fig. 1, the structures of N(-M)-A-S-H gels prepared via either ion-exchange or co-synthesis process are also non-crystalline and show broad amorphous humps centred at around 28–29° (2θ). However, compared with the N-A-S-H gels, the centres of the amorphous humps appeared in the two N(-M)-A-S-H samples prepared through ion-exchange are lower by approximately 1° (2θ), suggesting potential differences in the amorphous aluminosilicate structures. Similar changes were observed from N-A-S-H gels with cation site partially replaced by Ca^{2+} or Sr^{2+} (Walkley et al., 2019). With references to the standard XRD patterns shown at the bottom of Fig. 1, it suggests that $Mg(NO_3)_2$ hydrates and $Mg(OH)_2$ (potentially from synthesis process) were not observed from these samples. Fig. 2 illustrates the 2D schematic nanostructure of the sodium aluminosilicate hydrate N-A-S-H gels with the Si and Al atoms in tetrahedral coordination and hydrated Na^+ ions as extra-framework cations.

The bulk chemical compositions of the alkali aluminosilicate geopolymer gels investigated in this study are summarised in Table 2, together with the stoichiometric chemical formula converted from the characterised chemical compositions (excluding the content of water). The results shown are average chemical composition values obtained from 15 random locations, of which the standard deviations for all major elements are below 1.7 wt%. The results show that the experimentally

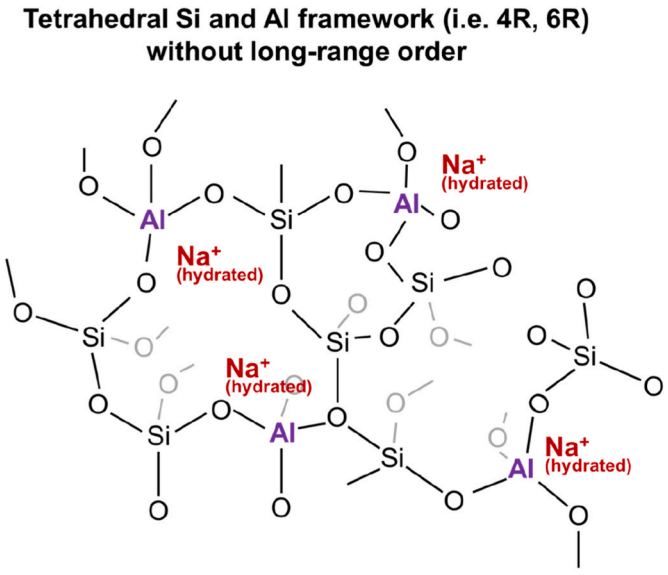

Fig. 2. A 2D schematic atomic structure of the sodium aluminosilicate hydrate N-A-S-H, with Si and Al in tetrahedral coordination and hydrated Na^+ ions as extra-framework cations. The presence of water is omitted from this plot, where 4R and 6R refer to four- and six-members aluminosilicate ring structures, respectively.

Table 1
Summary of chemical composition and structure parameters of the reference minerals.

Investigated by Si K-edge				
Minerals	Formula	Si–O connectivity	Bond distance $D_{Si\text{-}O}$ (Å)	Ref
Quartz	SiO_2	Q^4	1.609	Li et al. (1995a)
Silica gel	SiO_2	Q^4	1.610	Ohsaki et al. (1994)
Talc	$Mg_3Si_4O_{10}(OH)_2$	Q^3	1.623	Li et al. (1995a)
Syn. CaSiO3	$CaSiO_3$	Q^2	1.624	Yang and Prewitt (1999)
Investigated by Al K-edge				
Minerals	Formula	[a]CN	Bond distance $D_{Al\text{-}O}$ (Å)	Ref
Ye'elimite		4	1.740	(Cuesta et al., 2013; Liu et al., 2018)
Ettringite		6	1.850	Goetz-Neunhoeffer and Neubauer (2006)
Hydrotalcite	[a]$Mg_{0.7}Al_{0.3}$ $(OH)_2(CO_3)_{0.15}{\cdot}0.63H_2O$	6	1.820	van Bokhoven et al. (2001)
Investigated by Mg K-edge				
Minerals	Formula	CN	Bond distance $d_{Mg\text{-}O}$ (Å)	Ref
Talc	$Mg_3Si_4O_{10}(OH)_2$	6	2.071	Li et al. (1999)
Hydrotalcite	[b]$Mg_{0.7}Al_{0.3}$ $(OH)_2(CO_3)_{0.15}{\cdot}0.63H_2O$	6	2.066	Zhitova et al. (2018)
Dolomite	$CaMg(CO_3)_2$	6	2.082	Reeder and Markgraf (1986)
Periclase	MgO	6	2.105	(Hazen, 1976; Ildefonse et al., 1995)
Brucite	$Mg(OH)_2$	6	2.110	(LBNL Materials Project, 2020)

[a] CN = coordination number.
[b] Same as characterised in previous study(Ke et al., 2016).

Table 2
The average bulk chemical compositions (excluding water) measured using SEM-EDX analysis (15 data points with all standard deviations below 1.7 wt%) and the converted stoichiometric chemical formula. The raw materials and the synthetic aluminosilicate gels might contain trace impurities (<1.8 wt%, mainly TiO_2 attributed by anatase impurity from the metakaolin precursor).

Sample ID	Na_2O (wt.%)	MgO (wt.%)	Al_2O_3 (wt.%)	SiO_2 (wt.%)	Experimentally characterised stoichiometric chemical formula[b]
Metakaolin precursor	0.4	0.0	44.6	52.8	–
N-A-S-H1.5	16.6	0.0	31.0	51.9	$Na_2O{\cdot}Al_2O_3{\cdot}2.8SiO_2{\cdot}11H_2O$
N-A-S-H1.7	15.2	0.0	28.7	55.4	$Na_2O{\cdot}Al_2O_3{\cdot}3.3SiO_2{\cdot}11H_2O$
N(M)-A-S-H1.5	6.2	7.2	31.4	53.4	$0.4Na_2O{\cdot}0.6MgO{\cdot}Al_2O_3{\cdot}2.8SiO_2{\cdot}11H_2O$
N(M)-A-S-H1.7	7.7	4.6	29.7	56.9	$0.5Na_2O{\cdot}0.5MgO{\cdot}Al_2O_3{\cdot}3.3SiO_2{\cdot}11H_2O$
N(M)-A-S-H1.5-CoSyn	14.2	0.8[a]	31.5	52.9	$0.9Na_2O{\cdot}0.1MgO{\cdot}Al_2O_3{\cdot}2.8SiO_2{\cdot}11H_2O$

[a] The standard deviation from the SEM-EDX analysis for this element was 0.15%.
[b] The water content shown here are based on the designed values, not characterised.

characterised bulk Si/Al ratios of the synthetic sodium aluminosilicate hydrates (N-A-S-H) and Mg-substituted sodium aluminosilicate hydrates (N(-M)-A-S-H) are slightly lower than the initial stoichiometric design. For samples designed with Si/Al ratios of 1.5 and 1.7, the experimentally characterised Si/Al ratios are 1.40 and 1.65. This slight variation might be due to the presence of impurities in the sodium silicate solution used for preparing the activator. Sample N(-M)-A-S-H1.5 and N(-M)-A-S-H 1.7 were prepared by replacing the Na^+ in the N-A-S-H gels with Mg^{2+} through ion-exchange, where 60% and 50% of the original monovalent extra-framework cation locations (originally taken by Na^+) were replaced by divalent Mg^{2+} respectively. For N-A-S-H gels with higher Si/Al ratios, the aluminosilicate framework structure contains lower molar fraction of tetrahedrally coordinated Al and thus lower negative surface charge density, which might be responsible for the lower ion-exchange percentage observed from the high Si/Al ratio samples (Maes and Cremers, 1977). For the co-synthesised N(-M)-A-S-H gel, 10% of the negative charge was balanced by extra-framework Mg^{2+}, consistent with the initial stoichiometric design of the mixture used for co-synthesis. As no other Mg-bearing phases were identified from the co-synthesised N(-M)-A-S-H gel, it suggests that all of the Mg source remained as part of the amorphous aluminosilicate gels.

3.2. Si K-edge and Al K-edge XANES

Fig. 3 summarises the normalised Si K-edge XANES results of the reference minerals, N-A-S-H and N(-M)-A-S-H gels synthesised in this study. The quartz and silica gel are used as the reference for crystalline and amorphous Q^4(0Al) sites, and the synthetic $CaSiO_3$ and talc mineral are chosen as the reference for Q^3(0Al) and Q^2(0Al) sites. The Si–O bond length, bond angle, effective charge and degree of polymerization all have impacts on the structure of the Si K-edge XANES (Li et al., 1995a). The reference lines shown in Fig. 3 correspond to the structure features of standard quartz (Li et al., 1994). The peak A is attributed to the transition of Si ls electrons to the antibonding 3s-like state, which is forbidden by the dipole selection rules therefore only shown as a very weak absorption peak. The intense absorption peak B is assigned to the transition of Si ls electrons to the antibonding 3p-like state, which is normally used as the characteristic Si K-edge peak (Li et al., 1995a). Peaks D and F relate to transitions of electrons at higher coordination spheres, while the peaks C and E are attributable to the multiple scattering effect from outer shells (Li et al., 1994). The edge peak (peak B) energy values of the samples assessed in this study are summarised in Table 3.

The degree of silica(te) polymerization and the second-nearest atom of Si both affect the Si K-edge. Since amorphous silica and quartz have the same composition and degree of polymerization, their K-edge whiteline peak energies are nearly the same. The post-edge peaks of silica gel are nearly invisible in Fig. 3A compared to crystalline quartz as silica gel is poorly ordered. The lack of clear post-edge peaks is consistent with the studies of both nanocrystalline synthetic C–S–H and poorly crystalline hydration product C–S–H (Li et al., 2019b, 2021b). Heavier second-nearest neighbour element of the core Si results in less effective charge on Si slightly higher Si–O bond valence, and the decrease in electron shielding (more electronegativity) at higher degrees of silicate polymerization, and thus higher Si K-edge energy (Li et al., 1995a). This can explain the slightly lower or similar K-edge whiteline peak energy of Q^3 talc and Q^2 $CaSiO_3$ compared with Q^4 SiO_2. This phenomenon is also found in (Li et al., 2021b) where Q^2-Q^3 mixed tobermorite (Ca-bearing)

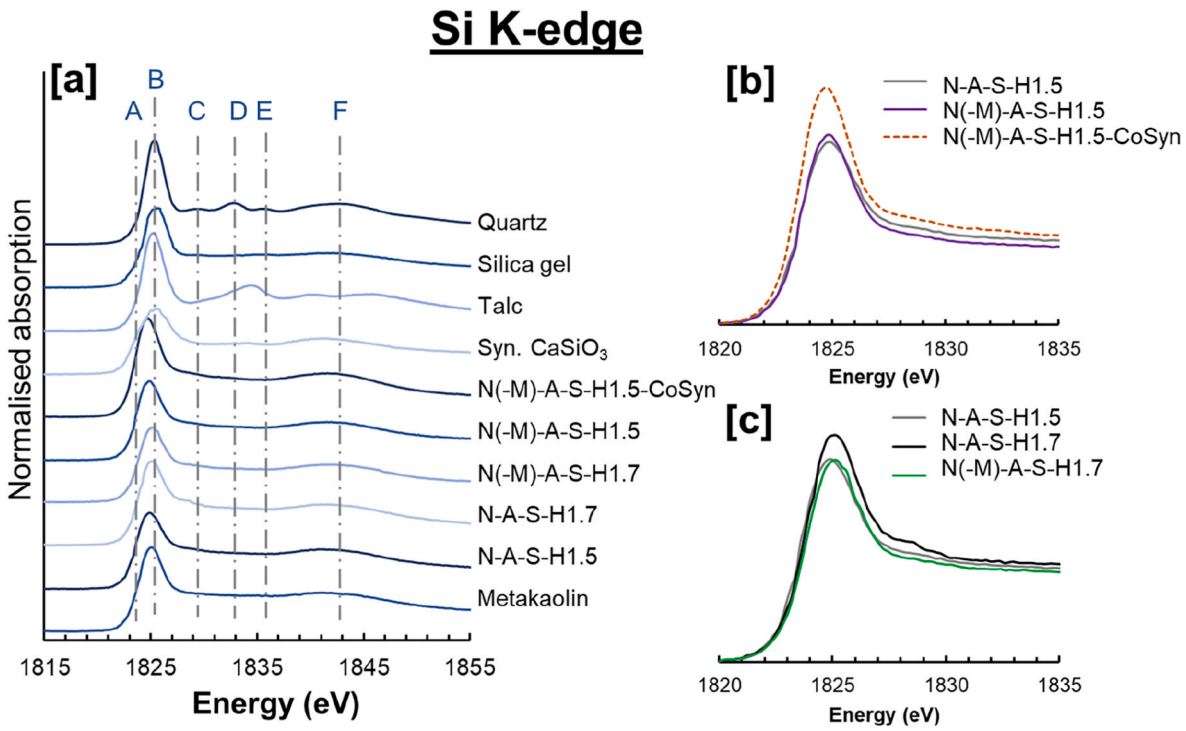

Fig. 3. (a) Normalised X-ray absorption spectra at the Si K-edge of investigated N-A-S-H gels, Mg-substituted N(-M)-A-S-H gels, and reference minerals in stacked plots. The reference lines A to F indicate the energy positions of structural features of quartz. (b) and (c) show the comparison of the near edge spectra of selected samples, normalised the same way as shown in (a).

Table 3
Summary of the K-edge whitline peak (peak B) energy of the Si K-edge XANES spectra shown in Fig. 3.

Sample	Peak energy (eV)
	Peak B (K-edge peak)
Metakaolin	1825.0
N-A-S-H1.5	1824.9
N-A-S-H1.7	1825.1
N(-M)-A-S-H1.5	1824.8
N(-M)-A-S-H1.7	1825.0
N(-M)-A-S-H1.5-CoSyn	1824.7
Quartz (Q^4(0Al), crystalline)	1825.3
Silica gel (Q^4(0Al), amorphous)	1825.5
Talc (Q^3(0Al))	1825.2
Syn. $CaSiO_3$ (Q^2(0Al))	1825.4

shows comparable Si K-edge to Q^3-Q^4 mixed metakaolin (Ca-free).

The Si K-edge XANES of metakaolin, N-A-S-H gels, and N(-M)-A-S-H gels exhibited similar absorption features as the silica gel, shown as an intense close-to-symmetric edge peak followed by a low intensity hump at about 16 eV above the edge peak (close to peak F). In comparison with silica gel, the edge peak energy of N-A-S-H and N(-M)-A-S-H gels are lower by about 0.4–0.8 eV. For both N-A-S-H and N(-M)-A-S-H gels, the decrease of bulk Si/Al ratio from 1.7 to 1.5 (increased Al substitution for Si) has also led to slight shift of the edge peak to lower energy. Considering the structural similarity of these phases, these energy shifts should predominately be attributed to the increased Al substitution for Si. The same effect was observed from the Si K-edge XANES spectra of natural silica and aluminosilicate minerals with varying bulk Si/Al ratios, where the increased Al substitution for Si reduces the effective charge on the Si atom (Li et al., 1995a). The Al substitution induced higher Si K-edge whiteline energy is consistent with previous comparisons with similar structures (Al-tobermorite versus tobermorite and C-A-S-H versus C–S–H) (Li et al., 2019a, 2021b). The broad hump feature was also observed from amorphous barium silicates which seem to be affected by the cations within the framework (Bender et al., 2002). The Si K-edge XANES confirms that the Si in metakaolin and the N-A-S-H gels (Fig. 2) are in tetrahedra coordination, in accordance with that characterised using the ^{29}Si solid-state NMR (Walkley et al., 2019, 2021). In comparison, the Si K-edge XANES of N(-M)-A-S-H gels prepared in this study also suggest Si solely in tetrahedral coordination, which further supported by the ^{29}Si solid-state NMR spectra of the ion-exchanged and co-synthesised N(-M)-A-S-H gels (at the Si/Al ratio of 1.5), shown in Figure S-4 in the Supporting Information document. The partial substitution of the extra-framework cation Na^+ by Mg^{2+} through ion-exchange seems to have negligible impact on the edge energy, with lower of peak energy by 0.1 eV (spectra step size 0.2 eV). The co-synthesised N(-M)-A-S-H showed a further decrease of the edge peak energy with an earlier rise of the edge. These slight energy shift might be due to weakening of the Si–O bond influenced by the changes of cation distributions in the second coordinate shells. The same effect was observed from sodium silicate glass with increased Na_2O content up to 30 wt% (Henderson, 1995), however this effect is normally much less significant for tetrahedral aluminosilicates (Li et al., 1995a).

Fig. 4 summarises the normalised Al K-edge XANES results of the reference minerals, N-A-S-H and N(-M)-A-S-H gels synthesised in this study, where the main absorption features can be observed within 25 eV above the absorption edge. The whiteline peak of the Al K-edge is related to the 1s to 3p transition (Ildefonse et al., 1998). The shift of the edge energy suggests changes in the average Al–O bond length, where in $Al^{[4]}$ the Al–O bond length is around 1.7 Å and that in $Al^{[6]}$ is around 1.9 Å (Ildefonse et al., 1998; Li et al., 1995b; van Bokhoven et al., 1999). Therefore, the K-edge whiteline peak energy differences between tetrahedrally coordinated $Al^{[4]}$ and octahedrally coordinated $Al^{[6]}$ are 2–3 eV, which has been recognised as fingerprint to determine the CN of Al (Ildefonse et al., 1998; Li et al., 1995b). As shown in Fig. 4, the reference line A indicates the edge energy of $Al^{[4]}$, while the reference line B indicates the edge energy of $Al^{[6]}$. The guide line C indicates the first resonance in the multiple scattering region for both $Al^{[4]}$ and $Al^{[6]}$ (Li et al., 1995b). The energy of edge peak and the first resonance of the

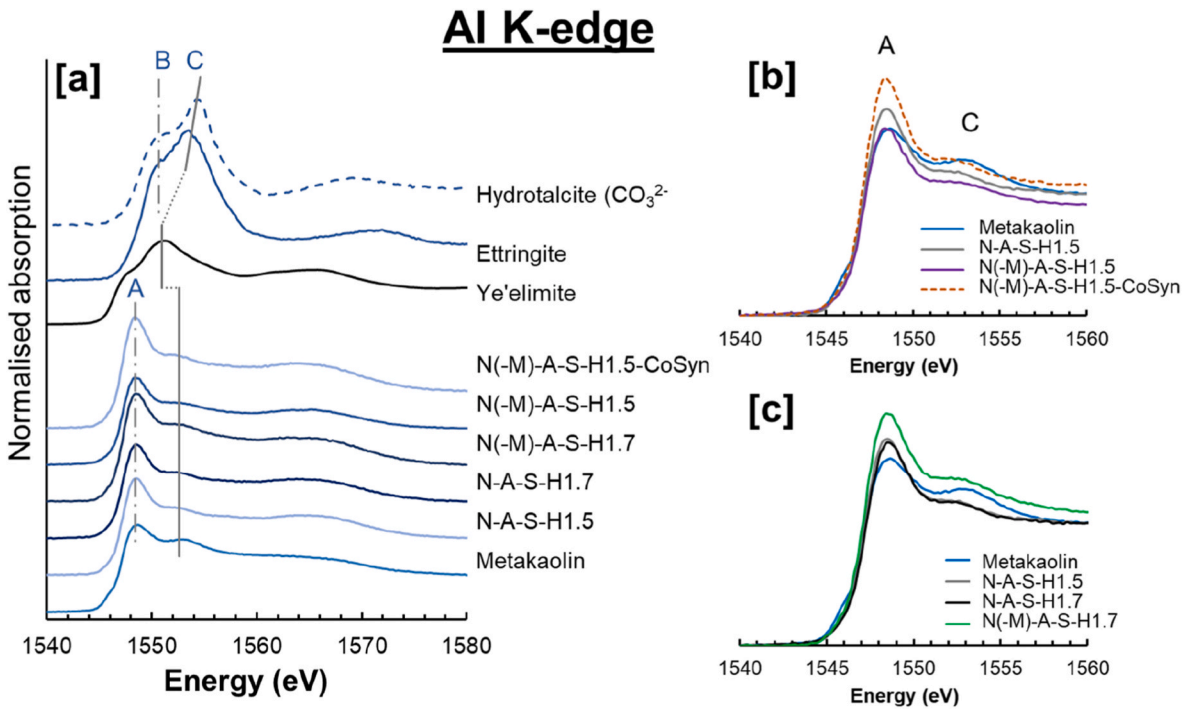

Fig. 4. (a) Normalised X-ray absorption spectra at the Al K-edge of investigated N-A-S-H gels, Mg-substituted N(-M)-A-S-H gels, and reference minerals in stacked plots. The reference line A (1547.8 eV) indicates the edge energy of $Al^{[4]}$, reference line B indicates the edge energy of $Al^{[6]}$, and reference line C indicates the secondary peak that appears in both $Al^{[4]}$ and $Al^{[6]}$ (Li et al., 1995b). (b) and (c) show the comparison of the near edge spectra of selected samples, normalised the same way as shown in (a).

results shown in Fig. 4 are summarised in Table 4.

For the reference minerals assessed in this study, the carbonated hydrotalcite and ettringite mineral should only contain octahedrally coordinated Al (Doyle et al., 1999; Skibsted et al., 2017), while ye'elimite contains only tetrahedrally coordinated Al (Paul et al., 2021; Pedersen et al., 2018). The carbonated hydrotalcite and ettringite showed a K-edge whiteline peak energy at 1550.9 eV and 1550.8 eV, respectively, followed by the first resonance peak with higher absorption intensity at 1554.4 eV and 1553.6 eV, consistent with that reported in the literature (van Bokhoven et al., 2001; Vespa et al., 2007; Wieland et al., 2010). The Al K-edge XANES results (relative peak positions and intensities) of hydrotalcite are also very close to that of gibbsite (Ildefonse et al., 1998) which contains distorted edge-sharing octahedral Al sites with Al–O distances between 1.83 Å to 1.95 Å (Saafeld and Wedde, 1974). This is also in agreement with the observation from the Mg–Al type layered double hydroxides, where the Al element substituting Mg in the brucite-like layers exhibits similar coordination environment to that of Al in gibbsite (Madej and Tyrała, 2020). The ye'elimite showed a K-edge energy at 1547.8 eV, about 3 eV lower than that of hydrotalcite and ettringite. The first resonance peak was observed at 1551.2 eV, matching with the fingerprint features of $Al^{[4]}$.

Metakaolin contains Al in both octahedral and tetrahedral coordination, and might also contain $Al^{[5]}$ (Walkley et al., 2019); however the latter is difficult to distinguish in the Al K-edge XANES data (Li et al., 1995b). Comparing metakaolin with the N-A-S-H the changes in the edge peak energy are negligible (0–0.1 eV); while compared with the N(-M)-A-S-H gels, the edge peak energy shifted to slightly lower energy (with 0.1–0.3 eV differences). The main difference appears as the reduction of peak C, which indicates the reduction of octahedral Al (van Bokhoven et al., 2003) as the results of the geopolymerisation process (Walkley et al., 2019). Between N-A-S-H gels with different bulk Si/Al ratios (Fig. 4C), the edge peak energy was the same, suggesting that the change of Si/Al bulk ratio between 1.5 and 1.7 might not lead to observable changes in the average Al–O bond length. This is consistent with that observed from feldspars minerals and aluminosilicate glass materials, where the second-shell atoms (Al–O-T[Si, Al]) does not seem to have noticeable contribution to the average Al–O bond length (Calas et al., 1987). Nevertheless, a slight energy shift was observed from the first resonance peak (peak C) of these two samples, which indicates that changes in second-shell arrangement would mainly impact the scatter path of the electrons (Ildefonse et al., 1998). Between N-A-S-H and N(-M)-A-S-H gels of the same bulk Si/Al ratio, the differences between their K-edge whiteline peak energy and first resonance peak energy are negligible (0–0.1 eV), except for the co-synthesised N(-M)-A-S-H (0.2 eV). The results shown in Fig. 4 suggest that the presence of Mg^{2+} in the extra-framework cation sites, introduced either through ion-exchange or co-synthesis process, does not have significant impact on the coordination environment of Al in the first coordination shell. It is also worth to note that the Al K-edge XANES spectrum of N-A-S-H gels characterised in this study showed very similar features to that of natrolite (zeolite with bulk Si/Al ratio of 1.5) in the regions about 30 eV above the edge energy (Ildefonse et al., 1998). This is in agreement with that characterised by ^{27}Al NMR, where the chemical shift of Al in N-A-S-H gels (Walkley et al.,

Table 4
Summary of the peak energy values of the Al K-edge XANES spectra shown in Fig. 4. The peak A correspond to the edge energy of $Al^{[4]}$, the peak B correspond to the edge energy of $Al^{[6]}$, while peak C correspond to the secondary peak that appears in both $Al^{[4]}$ and $Al^{[6]}$.

Sample	Peak energy (eV)		
	A	B	C
Metakaolin	1548.6	–	1553.3
N-A-S-H1.5	1548.5	–	1552.5
N-A-S-H1.7	1548.6	–	1552.5
N(M)-A-S-H1.5	1548.4	–	1552.6
N(M)-A-S-H1.7	1548.5	–	1552.6
N(M)-A-S-H1.5-CoSyn	1548.3	–	1551.9
Ye'elimite	1547.8	–	1551.2
Ettringite	–	1550.8	1553.6
Hydrotalcite (CO_3^{2-})		1550.9	1554.4

2021) are almost the same as that of sodium natrolite (Park et al., 2013). Combining with the Si K-edge XANES of the samples prepared in this study, it confirms that both the N-A-S-H and the N(-M)-A-S-H gels consist of tetrahedrally coordinated Si atoms within an aluminosilicate framework, with part of the tetrahedral Si sites substituted by Al, in accordance with that characterised using ^{27}Al and ^{29}Si solid state MAS NMR (Walkley et al., 2021).

3.3. Mg K-edge XANES

The Mg K-edge XANES spectra of the synthetic N(-M)-A-S-H gels and reference minerals, $Mg(NO_3)_2{\bullet}6H_2O$, carbonated hydrotalcite, talc, magnesium silicate hydrate (M-S-H, from (Vespa et al., 2020)), sodium- and aluminium-substituted magnesium silicate hydrate (M(-N)(-A)-S-H, from (Vespa et al., 2020)), are shown in Fig. 5. The $Mg(NO_3)_2{\bullet}6H_2O$ was used as a Mg donor during synthesis, the carbonated hydrotalcite is the most commonly identified Mg-bearing phase in the alkali-activated binder system (Bernal et al., 2014; Provis and Bernal, 2014). Talc has a similar chemical structure to the magnesium silicate hydrate (M-S-H) which is predicted to form in carbonated alkali-activated slags (Bernard et al., 2017; Ke et al., 2020; Vespa et al., 2020) and alkali-activated materials with medium CaO content but contains significant amount of MgO and aluminosilicate (Ke and Duan, 2021). All of the reference chemical and minerals investigated in this study have Mg in octahedral coordination (CN = 6, Table 1), which typically presents a triplet structure in the full multiple scattering zone at around 15 eV above the K-edge energy (G. Cibin et al., 2002; Li et al., 1999), labelled as peak A, B, and C (Fig. 5). Table 5 summarised the peak energy and relative peak intensities (after normalisation) of the results shown in Fig. 5 in the full multiple scattering zone, together with the corrected values of typical periclase (MgO), brucite ($Mg(OH)_2$), M-S-H and M(-N)(-A)-S-H from (Vespa et al., 2020) for comparison.

For Mg K-edge XANES, the peak A and peak C relate to the multiple scattering from the outermost coordination shells around the absorbing Mg, while the peak B related to the transition of ls to the empty bound 3p-like state within the first coordination sphere (Li et al., 1999). The peak D, E, F and G in the post-edge region are oscillations in the intermediate multiple scattering zone (Sánchez del Río et al., 2005; Vespa et al., 2017). Since no oxidation state change occurs for Mg, the energy shifts in the full multiple scattering zone should be attributed to changes in the bond length and/or bond angles due to different coordination geometries of Mg (Khamkongkaeo et al., 2018; Li et al., 1999; Sánchez del Río et al., 2005; Yoshimura et al., 2013). The energy shifts of both peak A and B are associated with changes in the average Mg–O bond length, where the decrease of Mg–O bond length in Mg-bearing polysilicate minerals resulted in the shift of peak B to higher energy (Li et al., 1999). As peak A, B and C relate to medium range ordering, the appearance of peak C is likely relating to the changes at the length of 6 Å away from the core Mg atom (Sánchez del Río et al., 2005). The loss of defined feature or absence of peak C is most likely due to changes in the second shell atoms. For polysilicate minerals, the decrease of bulk Si/Al ratio results in changes in the neighbouring Al within the aluminosilicate structure and appeared as reduction in the intensities of the peak C (Li et al., 1999; Vespa et al., 2020). In addition, the presence of Mg vacancies in a defect crystalline structure might also lead to decreased intensity of peak C (Sánchez del Río et al., 2005), as well as the amorphisation due to reduced crystallinity (Ildefonse et al., 1995).

Comparing the XANES spectra of the three N(-M)-A-S-H phases with the reference minerals (Fig. 5), it appears that the coordination environment of Mg in the N(-M)-A-S-H phase is most close to that in the talc. The peak A of M-S-H and M(-N)(-A)-S-H are slightly lower than talc, same as observed by Vespa et al. (2018), suggesting an intermediate structure between talc and brucite. However, comparing to the exact Mg K-edge spectrum of talc, slight shifts in peak energy and changes in relative peak intensities of peak A and B and significant broadening (or reduction) of peak C, E and F, can be observed from N(-M)-A-S-H phases. The $Mg(NO_3)_2{\bullet}6H_2O$ shows a dominate edge peak (peak A) at 1297.6 eV, about 1.0 eV higher than the other samples characterised, followed by a shoulder at 1301.2 eV (peak C). The carbonated hydrotalcite phase also presents a close-to-triplet structure within the full multiple scattering zone. However, in comparison with talc and brucite (with Mg in non-distorted octahedral coordination (Sánchez del Río et al., 2005)), the peak B of carbonated hydrotalcite has shifted to higher energy by 1.2 eV. The hydrotalcite contains Mg in brucite-like layers with part of

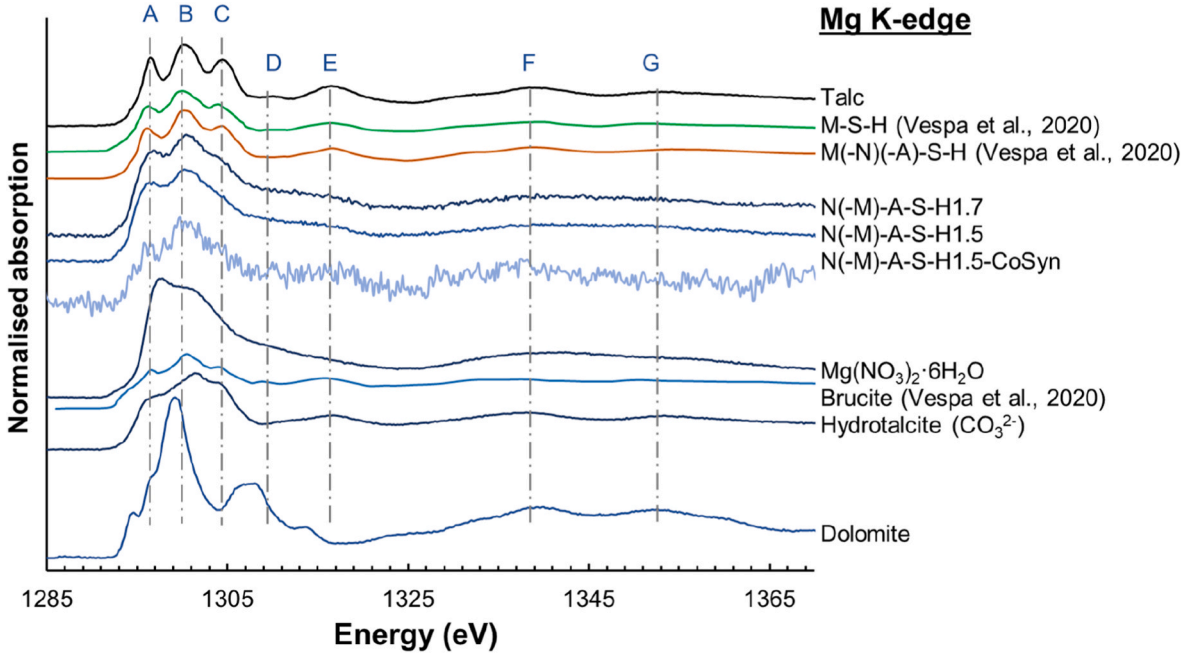

Fig. 5. Normalised X-ray absorption spectra at the Mg K-edge of investigated Mg-substituted N(-M)-A-S-H gels and reference minerals in stacked plots. The reference lines A to G indicate the energy position of structural features of talc. The spectrum of M-S-H (Mg/Si = 1), M(-N)(-A)-S-H (Mg/Si = 0.8 and Al/Si = 0.1) and brucite was reproduced from (Vespa et al., 2020) with the K-edge value corrected (matching the Mg K-edge of talc from both studies) for comparison.

Table 5
Summary of the peak energy values and relative intensities of the Mg K-edge XANES spectra shown in Fig. 5.

Sample	Peak energy (eV)				Relative intensity			
	Pre-edge	A	B	C	Pre-edge	A	B	C
N(M)-A-S-H1.5	–	1296.6	1300.5	–	–	2.84	3.38	–
N(M)-A-S-H1.7	–	1296.8	1300.6	1305.0 (shoulder)	–	3.07	3.68	2.58
N(M)-A-S-H1.5-CoSyn	–	1296.4 (estimated)	1300.2 (estimated)	–	–	1.69	2.58	–
Talc	–	1296.5	1300.2	1304.5	–	2.50	2.99	2.44
$Mg(NO_3)_2 \bullet 6H_2O$	–	1297.6	1301.2	–	–	4.33	3.95	–
Dolomite	1294.6	1296.7 (shoulder)	1299.2	–	1.66	2.99	5.91	–
Hydrotalcite (CO_3^{2-})	–	1296.4	1301.4	1304.1	–	1.89	2.85	2.48
[a]M-S-H (Mg/Si = 1) Vespa et al. (2020)	–	1296.3	1300.0	1304.0	–	1.74	2.30	1.80
[a]M(-N)(-A)-S-H (Mg/Si = 0.8 and Al/Si = 0.1) (Vespa et al., 2020)		1296.3	1300.2	1304.4	–	1.89	2.56	2.00
[a]Periclase (MgO) (Vespa et al., 2020)	–	1295.2	1301.0	1303.5	–	2.02	2.00	2.13
[a]Brucite ($Mg(OH)_2$) (Vespa et al., 2020)	1293.7	1296.5	1300.2	1304.3	0.65	1.52	2.13	1.64

[a] The peak energy of periclase and brucite are originally from (Vespa et al., 2020) but shown as corrected values using the K-edge energy of talc reported in (Vespa et al., 2020) and this study to enable direct comparison of the results.

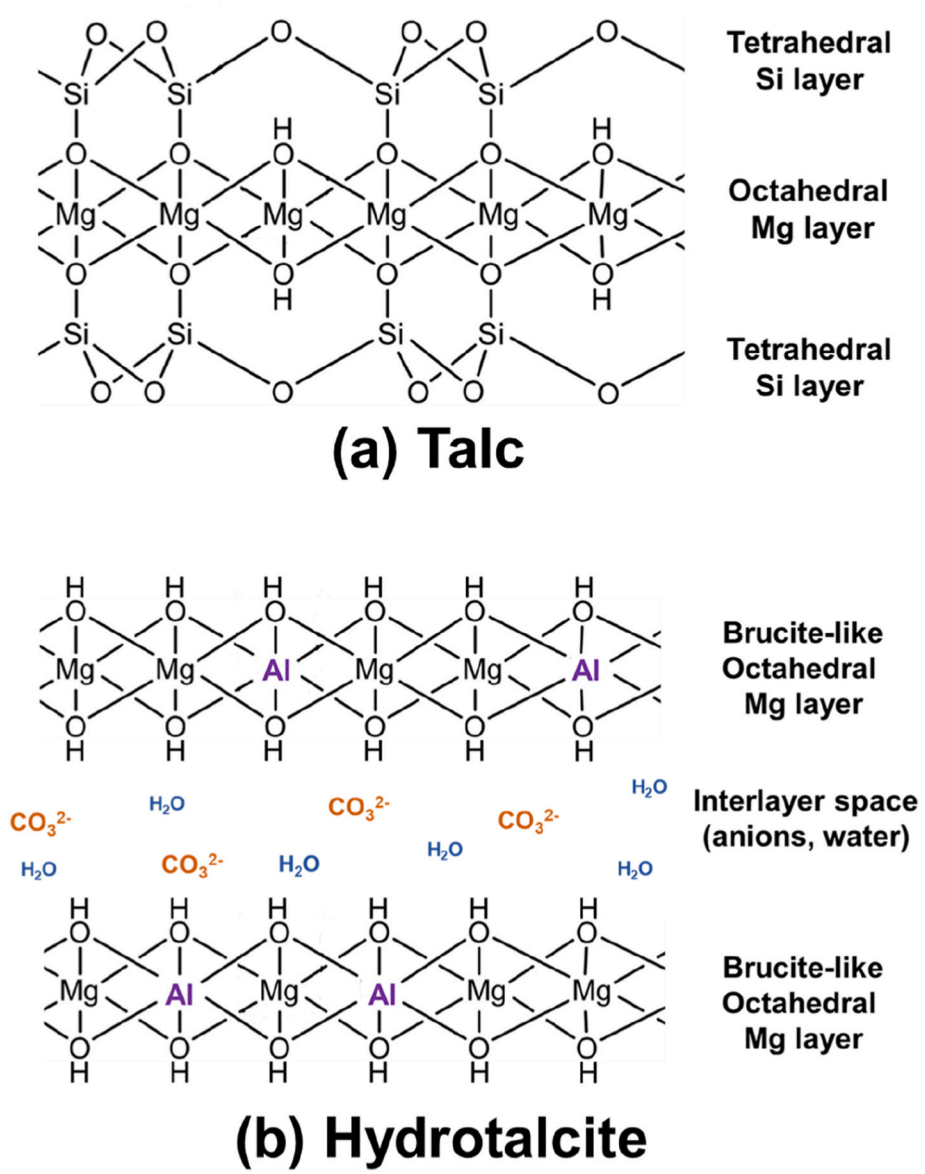

Fig. 6. 2D schematic crystal structure of (a) talc and (b) carbonated hydrotalcite.

the Mg (CN = 6) cites replaced by Al (Fig. 6b), where several different local Mg and Al distributions geometry might exist (Sideris et al., 2008). Comparing the XANES results of hydrotalcite and brucite (Table 5), it seems that the replace of nearby Mg (CN = 6) by Al in the brucite-like layer led to decrease of the average length of the Mg–O bond (Table 1), resulting in peak B shifting to higher energy. Comparing hydrotalcite with talc, the hydrotalcite (Fig. 6b) contains Mg–OH bonds in the brucite-like layer which might be influenced by neighbouring octahedral Al through edge sharing of the octahedral structure (van Bokhoven et al., 2001); however, talc (Fig. 6a) does not contain brucite-like layers and contains a fraction of Mg sites connecting to the silicate layers via corner sharing of the oxygen site (Mg–O–Si bonds) (Miehé-Brendlé et al., 2010). The differences between talc and hydrotalcite are similar to that reported for talc and brucite (Vespa et al., 2018), suggesting that the coordination geometries of Mg in hydrotalcite are closer to that in brucite but significantly different to that in talc.

Fig. 7 compares the Mg K-edge XANES results of the different N(-M)-A-S-H gels with that of talc, sodium and aluminium substituted magnesium silicate hydrate (M(-N)(-A)-S-H), and hydrotalcite in the full multiple scattering zone. For N(-M)-A-S-H obtained through ion-exchange (Fig. 7a), the most significant differences to that of talc are the increase of peak B energy by 0.3–0.4 eV while significantly reduced in the intensity of peak C. Ion-exchanged N(-M)-A-S-H with lower bulk Si/Al ratio (N(-M)-A-S-H1.5) showed slightly less energy increase for peak B (0.3 eV) but almost complete disappearance of peak C, similar to that observed from Mg-bearing aluminosilicate minerals and the Al substituted M-S-H gels (with Si mainly in Q^2 coordination) (Li et al., 1999; Vespa et al., 2020). This suggest that the coordination environment of Mg in N(-M)-A-S-H gels synthesised through ion-exchange might be very close to that in talc but with much less influence from the surrounding Si or Al atoms (second shell). This is consistent with Mg being in the role of extra-framework cations. The previous study on the N-A-S-H gels revealed that the extra-framework cation Na^+ are coordinated by both framework oxygen (T-O-T) and water hydrates (Walkley et al., 2018). As extra-framework cations with stronger coordination with the framework oxygen will be more difficult to be ion-exchanged (Cundy and Cox, 2005), the Na cation sites with weaker coordination with the framework oxygen will be readily replaced by the hydrated Mg cations. Therefore, the Mg in the N(-M)-A-S-H obtained through ion-exchange (Fig. 8a) has much less influence from the second shell atom Si (or Al) in comparison to talc (Fig. 6a). The reduction of peak C is most likely attributed by the amorphous nature of the surrounding aluminosilicate framework (random distribution of Al and Si) and the increased neighbouring Al (comparing to talc which contains no Al) (Ildefonse et al., 1995; Li et al., 1999; Vespa et al., 2020). Due to the low bulk Mg content in the co-synthesised N(-M)-A-S-H phase comparing to other Mg-bearing phases, its Mg K-edge XANES features are much less well-defined and suffers from noise interference from the environmental background (Fig. 7b). Comparing with sodium- and aluminium-substituted magnesium silicate hydrate (M(-N)(-A)-S-H), the positions of peak A and peak B of the co-synthesised N(-M)-A-S-H phase are very similar, but also with the absence of peak C. This suggest that the coordination environment of Mg in the co-synthesised N(-M)-A-S-H gel is closer to that in the M(-N)(-A)-S-H, with stronger influences from the surrounding second shell atoms (i.e., Si and Al) comparing to that in the ion-exchanged N(-M)-A-S-H gels. Therefore, Mg introduced through co-synthesis is likely to have higher number of coordination with the framework oxygen (Fig. 8b) than that of the Mg incorporated through ion-exchanged (Fig. 8a).

4. Conclusions

Compared with standard reference minerals, i.e., quartz (Q^4 Si), silicate gel (amorphous Q^4 Si), talc (Q^3 Si), Ye'elimite ($^{[4]}$Al), ettringite and hydrotalcite ($^{[6]}$Al), the Si and Al K-edge XANES results of N-A-S-H gels with different Si/Al ratios show that the Si and Al atoms are both in tetrahedral coordination. The increase of bulk Si/Al ratio leads to slight increase of Si K-edge whiteline peak energy (less effective charge on Si) while having negligible impact on the Al K-edge whiteline peak energy (similar Al coordination environment). Comparing to the N-A-S-H gels with the same bulk Si/Al ratio, the substitution of Mg in the N-A-S-H gel, either through co-synthesis or ion-exchange, leads to slightly lower Si and Al K-edge whiteline peak energy indicating negligible changes in the coordination environment. The XANES results at Si and Al K-edge are consistent with existing NMR results. The Mg K-edge XANES results show that the Mg in the N(-M)-A-S-H gels, either introduced to N-A-S-H through ion-exchange or co-synthesis process, is in octahedral coordination (CN = 6). The coordination environment of these Mg atoms is closer to Mg in talc instead of in brucite-like structure (hydrotalcite). However, comparing with talc, the Mg atoms in N(-M)-A-S-H gels contain higher number of Mg–OH bonds and thus less influence from the neighbouring Si and Al atoms, shown as shift of peak B to higher energy and absence of peak C. Comparing with the carbonated hydrotalcite, the energy of peak B in the Mg-substituted alkali aluminosilicate is lower by around 0.8–1.2 eV, which can be used as the fingerprint to probe the existence of N(-M)-A-S-H gels in alkali-activated geopolymer materials containing Mg. The absorption features of these phases are valuable for identifying complexes and phases in heterogenous cement/binder systems using micro-XAS, scanning transmission X-ray microscopy, and other XAS spectromicroscopy.

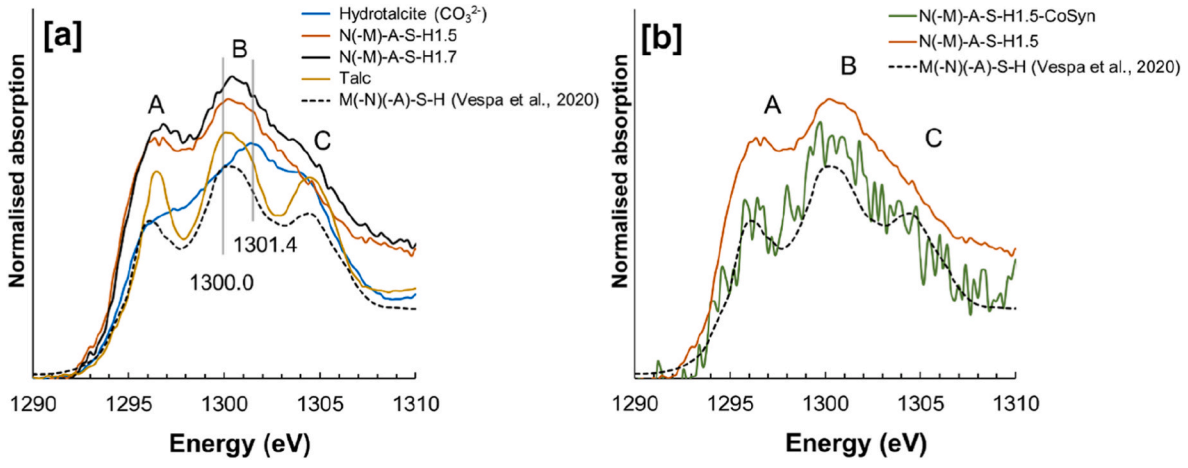

Fig. 7. Comparison of the near edge Mg K-edge spectra of the N(-M)-A-S-H samples with hydrotalcite, talc, and M(-N)(-A)-S-H (reproduced from (Vespa et al., 2020)) the presented spectra were normalised the same way as shown in Fig. 5.

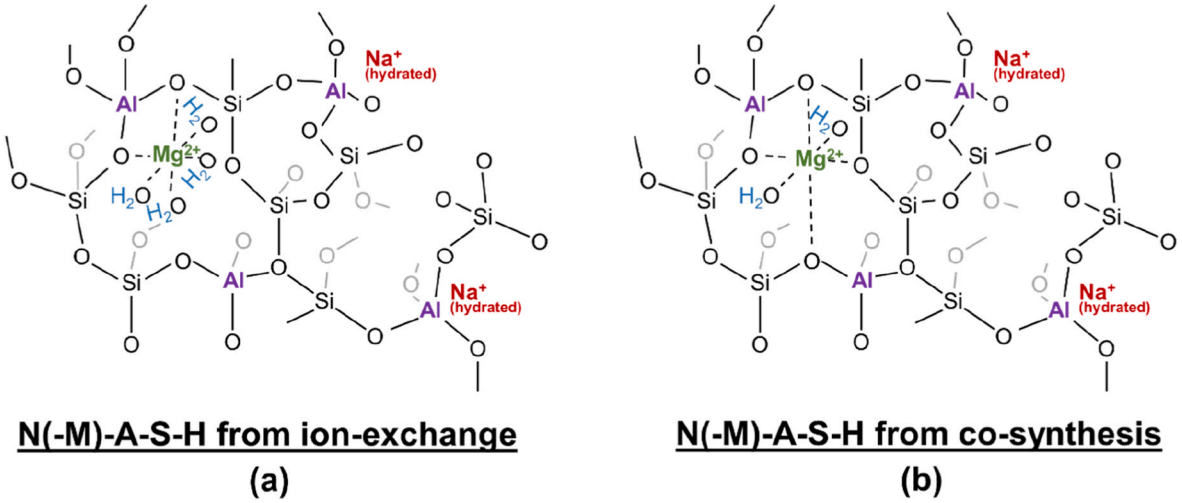

Fig. 8. 2D schematic atomic structure of Mg-substituted alkali aluminosilicate hydrates N(-M)-A-S-H prepared from (a) ion-exchange, (b) co-synthesis.

Declaration of competing interest

The authors declare that they have no known competing financial interests or personal relationships that could have appeared to influence the work reported in this paper.

Data availability

Data will be made available on request.

Acknowledgement

This work was carried out with the support of Diamond Light Source, instrument B07 (proposal SI28470). This research was partially funded by the UK Engineering and Physical Sciences Research Council (EPSRC) through Grant EP/W010828/1. The participation of XK was partially funded by the University of Bath Prize Fellowship (2018–2021). The participation of JL was under the auspices of the U.S. Department of Energy by Lawrence Livermore National Laboratory (contract No. DE-AC52-07NA27344), with LLNL IM release number LLNL-JRNL-833223. The authors would also like to thank Imerys (UK) for supplying metakaolin materials for this study. The authors would also like to acknowledge Dr Daniel Geddes, The University of Sheffield, for assisting the collection of ^{29}Si solid-state MAS NMR data (included in Supplementary data).

Appendix A. Supplementary data

Supplementary data to this article can be found online at https://doi.org/10.1016/j.apgeochem.2022.105515.

References

Bender, S., Franke, R., Hartmann, E., Lansmann, V., Jansen, M., Hormes, J., 2002. X-ray absorption and photoemission electron spectroscopic investigation of crystalline and amorphous barium silicates. J. Non-Cryst. Solids 298, 99–108.
Bernal, S.A., Provis, J.L., Walkley, B., San Nicolas, R., Gehman, J.D., Brice, D.G., Kilcullen, A.R., Duxson, P., van Deventer, J.S.J., 2013. Gel nanostructure in alkali-activated binders based on slag and fly ash, and effects of accelerated carbonation. Cement Concr. Res. 53, 127–144.
Bernal, S.A., San Nicolas, R., Myers, R.J., Mejía de Gutiérrez, R., Puertas, F., van Deventer, J.S.J., Provis, J.L., 2014. MgO content of slag controls phase evolution and structural changes induced by accelerated carbonation in alkali-activated binders. Cement Concr. Res. 57, 33–43.
Bernard, E., Lothenbach, B., Rentsch, D., Pochard, I., Dauzères, A., 2017. Formation of magnesium silicate hydrates (M-S-H). Phys. Chem. Earth, Parts A/B/C 99, 142–157.
Calas, G., Brown, G.E., Waychunas, G.A., Petiau, J., 1987. X-ray absorption spectroscopic studies of silicate glasses and minerals. Phys. Chem. Miner. 15, 19–29.
Cibin, G., Marcelli, A., Mottana, A., Giuli, G., Della Ventura, G., Romano, C., Paris, E., Cardelli, A., Tombolini, F., 2002. Magnesium X-Ray Absorption Near-Edge, 19th International Conference on X-Ray and Inner Shell Processes (Roma).
Cuesta, A., De la Torre, A.G., Losilla, E.R., Peterson, V.K., Rejmak, P., Ayuela, A., Frontera, C., Aranda, M.A.G., 2013. Structure, atomistic simulations, and phase transition of stoichiometric yeelimite. Chem. Mater. 25, 1680–1687.
Cundy, C.S., Cox, P.A., 2005. The hydrothermal synthesis of zeolites: precursors, intermediates and reaction mechanism. Microporous Mesoporous Mater. 82, 1–78.
Doyle, C.S., Traina, S.J., Ruppert, H., Kendelewicz, T., Rehr, J.J., Brown Jr., G.E., 1999. XANES studies at the Al K-edge of aluminium-rich surface phases in the soil environment. J. Synchrotron Radiat. 6, 621–623.
García-Lodeiro, I., Fernández-Jiménez, A., Palomo, A., Macphee, D.E., 2010. Effect of calcium additions on N–A–S–H cementitious gels. J. Am. Ceram. Soc. 93, 1934–1940.
Garcia-Lodeiro, I., Palomo, A., Fernández-Jiménez, A., Macphee, D.E., 2011. Compatibility studies between N-A-S-H and C-A-S-H gels. Study in the ternary diagram Na2O–CaO–Al2O3–SiO2–H2O. Cement Concr. Res. 41, 923–931.
Ge, Y., Yuan, Y., Wang, K., He, Y., Cui, X., 2015. Preparation of geopolymer-based inorganic membrane for removing Ni2+ from wastewater. J. Hazard Mater. 299, 711–718.
Geng, G., Myers, R.J., Yu, Y.-S., Shapiro, D.A., Winarski, R., Levitz, P.E., Kilcoyne, D.A.L., Monteiro, P.J.M., 2018. Synchrotron X-ray nanotomographic and spectromicroscopic study of the tricalcium aluminate hydration in the presence of gypsum. Cement Concr. Res. 111, 130–137.
Goetz-Neunhoeffer, F., Neubauer, J., 2006. Refined ettringite (Ca6Al2(SO4)3(OH)12•26H2O) structure for quantitative X-ray diffraction analysis. Powder Diffr. 21, 4–11.
Hazen, R.M., 1976. Effects of temperature and pressure on the cell dimension and X-ray temperature factors of periclase. Am. Mineral. 61, 266–271.
Held, G., Venturini, F., Grinter, D.C., Ferrer, P., Arrigo, R., Deacon, L., Quevedo Garzon, W., Roy, K., Large, A., Stephens, C., Watts, A., Larkin, P., Hand, M., Wang, H., Pratt, L., Mudd, J.J., Richardson, T., Patel, S., Hillman, M., Scott, S., 2020. Ambient-pressure endstation of the versatile soft X-ray (VerSoX) beamline at Diamond Light source. J. Synchrotron Radiat. 27, 1153–1166.
Henderson, G.S., 1995. A Si K-edge EXAFS/XANES study of sodium silicate glasses. J. Non-Cryst. Solids 183, 43–50.
Ildefonse, P., Calas, G., Flank, A.M., Lagarde, P., 1995. Low Z elements (Mg, Al, and Si) K-edge X-ray absorption spectroscopy in minerals and disordered systems. Nucl. Instrum. Methods Phys. Res. Sect. B Beam Interact. Mater. Atoms 97, 172–175.
Ildefonse, P., Cabaret, D., Sainctavit, P., Calas, G., Flank, A.M., Lagarde, P., 1998. Aluminium X-ray absorption Near Edge Structure in model compounds and Earth's surface minerals. Phys. Chem. Miner. 25, 112–121.
Ke, X., Baki, V.A., 2021. Assessing the suitability of alkali-activated metakaolin geopolymer for thermochemical heat storage. Microporous Mesoporous Mater. 325, 111329.
Ke, X., Duan, Y., 2021. Coupling machine learning with thermodynamic modelling to develop a composition-property model for alkali-activated materials. Compos. B Eng. 216, 108801.
Ke, X., Bernal, S.A., Provis, J.L., 2016. Controlling the reaction kinetics of sodium carbonate-activated slag cements using calcined layered double hydroxides. Cement Concr. Res. 81, 24–37.
Ke, X., Bernal, S.A., Sato, T., Provis, J.L., 2019. Alkali aluminosilicate geopolymers as binders to encapsulate strontium-selective titanate ion-exchangers. Dalton Trans. 48, 12116–12126.
Ke, X., Bernal, S.A., Provis, J.L., Lothenbach, B., 2020. Thermodynamic modelling of phase evolution in alkali-activated slag cements exposed to carbon dioxide. Cement Concr. Res. 136, 106158.

Khalifa, A.Z., Cizer, Ö., Pontikes, Y., Heath, A., Patureau, P., Bernal, S.A., Marsh, A.T.M., 2020. Advances in alkali-activation of clay minerals. Cement Concr. Res. 132, 106050.
Khamkongkaeo, A., Klysubun, W., Boonchuduang, T., Sailuam, W., Sriwattana, P., Phetrattanarangsi, T., Srimongkon, K., Sakkomolsri, B., Pimsawat, A., Daengsakul, S., Kidkhunthod, P., Bootchanont, A., Lohwongwatana, B., 2018. X-ray absorption spectroscopy investigation of relationship between Mg vacancy and magnetic properties of MgO powder. J. Magn. Magn Mater. 460, 327–333.
LBNL Materials Project, 2020. In: LBNL), L.B.N.L. (Ed.), Materials Data on $Mg(HO)_2$ by Materials Project. Berkeley, CA, United States.
Li, D., Bancroft, G.M., Kasrai, M., Fleet, M.E., Secco, R.A., Feng, X.H., Tan, K.H., Yang, B. X., 1994. X-ray absorption spectroscopy of silicon dioxide (SiO2) polymorphs: the structural characterization of opal. Am. Mineral. 79, 622–632.
Li, D., Bancroft, G.M., Fleet, M.E., Feng, X.H., 1995a. Silicon K-edge XANES spectra of silicate minerals. Phys. Chem. Miner. 22, 115–122.
Li, D., Bancroft, G.M., Fleet, M.E., Feng, X.H., Pan, Y., 1995b. Al K-edge XANES spectra of aluminosilicate minerals. Am. Mineral. 80, 432–440.
Li, D., Peng, M., Murata, T., 1999. Coordination and local structure of magnesium in silicate minerals and glasses; Mg K-edge XANES study. Can. Mineral. 37, 199–206.
Li, J., Geng, G., Myers, R., Yu, Y.-S., Shapiro, D., Carraro, C., Maboudian, R., Monteiro, P. J.M., 2019a. The chemistry and structure of calcium (alumino) silicate hydrate: a study by XANES, ptychographic imaging, and wide- and small-angle scattering. Cement Concr. Res. 115, 367–378.
Li, J., Geng, G., Zhang, W., Yu, Y.-S., Shapiro, D.A., Monteiro, P.J.M., 2019b. The hydration of β- and α′H-dicalcium silicates: an X-ray spectromicroscopic study. ACS Sustainable Chem. Eng. 7, 2316–2326.
Li, J., Zhang, W., Monteiro, P.J.M., 2020. Structure and intrinsic mechanical properties of nanocrystalline calcium silicate hydrate. ACS Sustainable Chem. Eng. 8, 12453–12461.
Li, C., Li, J., Telesca, A., Marchon, D., Xu, K., Marroccoli, M., Jiang, Z., Monteiro, P.J.M., 2021a. Effect of polycarboxylate ether on the expansion of ye'elimite hydration in the presence of anhydrite. Cement Concr. Res. 140, 106321.
Li, J., Zhang, W., Garbev, K., Monteiro, P.J.M., 2021b. Coordination environment of Si in calcium silicate hydrates, silicate minerals, and blast furnace slags: a XANES database. Cement Concr. Res. 143, 106376.
Liu, S., Lu, X., Chen, J., Wang, S., Ye, Z., Cheng, X., 2018. Modulation of two ye'elimite phases via Ga3+ cation substitution. CrystEngComm 20, 3755–3764.
Longhi, M.A., Rodríguez, E.D., Walkley, B., Eckhard, D., Zhang, Z., Provis, J.L., Kirchheim, A.P., 2022. Metakaolin-based geopolymers: efflorescence and its effect on microstructure and mechanical properties. Ceram. Int. 48, 2212–2229.
Luukkonen, T., Heponiemi, A., Runtti, H., Pesonen, J., Yliniemi, J., Lassi, U., 2019. Application of alkali-activated materials for water and wastewater treatment: a review. Rev. Environ. Sci. Biotechnol. 18, 271–297.
Madej, D., Tyrała, K., 2020. In situ spinel formation in a smart nano-structured matrix for No-cement refractory castables. Materials 13, 1403.
Maes, A., Cremers, A., 1977. Charge density effects in ion exchange. Part 1.-Heterovalent exchange equilibria. J. Chem. Soc., Faraday Trans. 1: Phys. Chemi. Condensed Phase. 73, 1807–1814.
Miehé-Brendlé, J., Tuilier, M.-H., Marichal, C., Gallego, J.-C., Reinholdt, M., 2010. Mg environments in the octahedral sheet of 2:1 talc-like hybrid phyllosilicates: a comparative xafs study, 2010 Eur. J. Inorg. Chem. 5587–5591.
Myers, R.J., Geng, G., Li, J., Rodríguez, E.D., Ha, J., Kidkhunthod, P., Sposito, G., Lammers, L.N., Kirchheim, A.P., Monteiro, P.J.M., 2017. Role of adsorption phenomena in cubic tricalcium aluminate dissolution. Langmuir 33, 45–55.
Ohsaki, H., Miura, K., Imai, A., Tada, M., Aegerter, M.A., 1994. Structural analysis of SiO2 gel films by high energy electron diffraction. J. Sol. Gel Sci. Technol. 2, 245–249.
Park, M.B., Vicente, A., Fernandez, C., Hong, S.B., 2013. Solid-state NMR study of various mono- and divalent cation forms of the natural zeolite natrolite. Phys. Chem. Chem. Phys. 15, 7604–7612.
Paul, G., Boccaleri, E., Cassino, C., Gastaldi, D., Buzzi, L., Canonico, F., Marchese, L., 2021. Fingerprinting the hydration products of hydraulic binders using snapshots from time-resolved in situ multinuclear MAS NMR spectroscopy. J. Phys. Chem. C 125, 9261–9272.
Pedersen, M.T., Jensen, F., Skibsted, J., 2018. Structural investigation of ye'elimite, Ca4Al6O12SO4, by 27Al MAS and MQMAS NMR at different magnetic fields. J. Phys. Chem. C 122, 12077–12089.
Provis, J.L., Bernal, S.A., 2014. Geopolymers and related alkali-activated materials. Annu. Rev. Mater. Res. 44, 299–327.
Provis, J.L., Lukey, G.C., van Deventer, J.S.J., 2005. Do geopolymers actually contain nanocrystalline zeolites? A reexamination of existing results. Chem. Mater. 17, 3075–3085.
Provis, J.L., Palomo, A., Shi, C., 2015. Advances in understanding alkali-activated materials. Cement Concr. Res. 78, 110–125. Part A.
Reeder, R.J., Markgraf, S.A., 1986. High-temperature crystal chemistry of dolomite. Am. Mineral. 71, 795–804.
Saafeld, H., Wedde, M., 1974. Refinement of the crystal structure of gibbsite, Al(OH)3. Z. Kristallogr. 139, 129–135.
Sánchez del Río, M., Suárez, M., García Romero, E., Alianelli, L., Felici, R., Martinetto, P., Dooryhée, E., Reyes-Valerio, C., Borgatti, F., Doyle, B., Giglia, A., Mahne, N., Pedio, M., Nannarone, S., 2005. Mg K-edge XANES of sepiolite and palygorskite. Nucl. Instrum. Methods Phys. Res. Sect. B Beam Interact. Mater. Atoms 238, 55–60.
Sideris, P.J., Nielsen, U.G., Gan, Z., Grey, C.P., 2008. Mg/Al ordering in layered double hydroxides revealed by multinuclear NMR spectroscopy. Science 321, 113–117.
Skibsted, J., Pedersen, M.T., Holzinger, J., 2017. Resolution of the two aluminum sites in ettringite by 27Al MAS and MQMAS NMR at very high magnetic field (22.3 T). J. Phys. Chem. C 121, 4011–4017.
Sreenivasan, H., Adesanya, E., Niu, H., Perumal, P., Kantola, A.M., Telkki, V.-V., Huttula, M., Cao, W., Provis, J.L., Illikainen, M., Kinnunen, P., 2021. Evidence of formation of an amorphous magnesium silicate (AMS) phase during alkali activation of (Na-Mg) aluminosilicate glasses. Cement Concr. Res. 145, 106464.
van Bokhoven, J.A., Sambe, H., Ramaker, D.E., Koningsberger, D.C., 1999. Al K-edge near-edge X-ray absorption fine structure (NEXAFS) study on the coordination structure of aluminum in minerals and Y zeolites. J. Phys. Chem. B 103, 7557–7564.
van Bokhoven, J.A., Roelofs, J.C.A.A., de Jong, K.P., Koningsberger, D.C., 2001. Unique structural properties of the Mg–Al hydrotalcite solid base catalyst: an in situ study using Mg and Al K-edge XAFS during calcination and rehydration. Chem. Eur J. 7, 1258–1265.
van Bokhoven, J.A., van der Eerden, A.M.J., Koningsberger, D.C., 2003. Three-coordinate aluminum in zeolites observed with in situ X-ray absorption near-edge spectroscopy at the Al K-edge: flexibility of aluminum coordinations in zeolites. J. Am. Chem. Soc. 125, 7435–7442.
Vespa, M., Wieland, E., Dähn, R., Grolimund, D., Scheidegger, A.M., 2007. Determination of the elemental distribution and chemical speciation in highly heterogeneous cementitious materials using synchrotron-based micro-spectroscopic techniques. Cement Concr. Res. 37, 1473–1482.
Vespa, M., Dähn, R., Huthwelker, T., Wieland, E., 2017. Soft X-ray absorption near-edge investigations of Mg-containing mineral phases relevant for cementitious materials. Phys. Chem. Earth, Parts A/B/C 99, 168–174.
Vespa, M., Lothenbach, B., Dähn, R., Huthwelker, T., Wieland, E., 2018. Characterisation of magnesium silicate hydrate phases (M-S-H): a combined approach using synchrotron-based absorption-spectroscopy and ab initio calculations. Cement Concr. Res. 109, 175–183.
Vespa, M., Borca, C., Huthwelker, T., Lothenbach, B., Dähn, R., Wieland, E., 2020. Structural characterisation of magnesium (sodium) aluminium silicate hydrate (M-(N)-A-S-H) phases by X-ray absorption near-edge spectroscopy. Appl. Geochem. 123, 104750.
Walkley, B., Rees, G.J., San Nicolas, R., van Deventer, J.S.J., Hanna, J.V., Provis, J.L., 2018. New structural model of hydrous sodium aluminosilicate gels and the role of charge-balancing extra-framework Al. J. Phys. Chem. C 122, 5673–5685.
Walkley, B., Ke, X., Hussein, O.H., Bernal, S.A., Provis, J.L., 2019. Incorporation of strontium and calcium in geopolymer gels. J. Hazard Mater., 121015
Walkley, B., Ke, X., Hussein, O., Provis, J.L., 2021. Thermodynamic properties of sodium aluminosilicate hydrate (N–A–S–H). Dalton Trans. 50, 13968–13984.
White, C.E., Provis, J.L., Proffen, T., Van Deventer, J.S.J., 2010. The effects of temperature on the local structure of metakaolin-based geopolymer binder: a neutron pair distribution function investigation. J. Am. Ceram. Soc. 93, 3486–3492.
Wieland, E., Dähn, R., Vespa, M., Lothenbach, B., 2010. Micro-spectroscopic investigation of Al and S speciation in hardened cement paste. Cement Concr. Res. 40, 885–891.
Yang, H., Prewitt, C.T., 1999. Crystal structure and compressibility of a two-layer polytype of pseudowollastonite (CaSiO 3). Am. Mineral. 84, 1902–1905.
Yang, T., Zhang, Z., Zhu, H., Gao, X., Dai, C., Wu, Q., 2019. Re-examining the suitability of high magnesium nickel slag as precursors for alkali-activated materials. Construct. Build. Mater. 213, 109–120.
Yoshimura, T., Tamenori, Y., Iwasaki, N., Hasegawa, H., Suzuki, A., Kawahata, H., 2013. Magnesium K-edge XANES spectroscopy of geological standards. J. Synchrotron Radiat. 20, 734–740.
Zhang, X., Bai, C., Qiao, Y., Wang, X., Jia, D., Li, H., Colombo, P., 2021. Porous geopolymer composites: a review. Compos. Appl. Sci. Manuf. 150, 106629.
Zhitova, E.S., Krivovichev, S.V., Yakovenchuk, V.N., Ivanyuk, G.Y., Pakhomovsky, Y.A., Mikhailova, J.A., 2018. Crystal chemistry of natural layered double hydroxides: 4. Crystal structures and evolution of structural complexity of quintinite polytypes from the Kovdor alkaline-ultrabasic massif, Kola peninsula, Russia. Mineral. Mag. 82, 329–346.